

Aberystwyth University

C1XS results - First measurement of enhanced Sodium on the Lunar surface

Athiray, P. S.; Narendranath, S.; Sreekumar, P.; Grande, Manuel

Published in:
Planetary and Space Science

DOI:
[10.1016/j.pss.2014.10.010](https://doi.org/10.1016/j.pss.2014.10.010)

Publication date:
2014

Citation for published version (APA):

Athiray, P. S., Narendranath, S., Sreekumar, P., & Grande, M. (2014). C1XS results - First measurement of enhanced Sodium on the Lunar surface. *Planetary and Space Science*, 104(Part B), 279-287.
<https://doi.org/10.1016/j.pss.2014.10.010>

General rights

Copyright and moral rights for the publications made accessible in the Aberystwyth Research Portal (the Institutional Repository) are retained by the authors and/or other copyright owners and it is a condition of accessing publications that users recognise and abide by the legal requirements associated with these rights.

- Users may download and print one copy of any publication from the Aberystwyth Research Portal for the purpose of private study or research.
- You may not further distribute the material or use it for any profit-making activity or commercial gain
- You may freely distribute the URL identifying the publication in the Aberystwyth Research Portal

Take down policy

If you believe that this document breaches copyright please contact us providing details, and we will remove access to the work immediately and investigate your claim.

tel: +44 1970 62 2400
email: is@aber.ac.uk

Author's Accepted Manuscript

C1XS results - First measurement of enhanced Sodium on the Lunar surface

P.S. Athiray, S. Narendranath, P. Sreekumar, M. Grande



www.elsevier.com/locate/pss

PII: S0032-0633(14)00323-7
DOI: <http://dx.doi.org/10.1016/j.pss.2014.10.010>
Reference: PSS3836

To appear in: *Planetary and Space Science*

Received date: 19 April 2014
Revised date: 14 October 2014
Accepted date: 17 October 2014

Cite this article as: P.S. Athiray, S. Narendranath, P. Sreekumar, M. Grande, C1XS results - First measurement of enhanced Sodium on the Lunar surface, *Planetary and Space Science*, <http://dx.doi.org/10.1016/j.pss.2014.10.010>

This is a PDF file of an unedited manuscript that has been accepted for publication. As a service to our customers we are providing this early version of the manuscript. The manuscript will undergo copyediting, typesetting, and review of the resulting galley proof before it is published in its final citable form. Please note that during the production process errors may be discovered which could affect the content, and all legal disclaimers that apply to the journal pertain.

C1XS results - First measurement of enhanced Sodium on the Lunar surface

P.S. Athiray^{a,b,**}, S. Narendranath^a, P. Sreekumar^c, M. Grande^d

^a*ISRO Satellite Centre, Vimanapura P.O., Bangalore 560 017, India*

^b*Department of Physics, University of Calicut, Thenjippalam, Kerala, India*

^c*Indian Institute of Astrophysics, Koramangala, Bangalore, India*

^d*Institute of Mathematics, Physics and Computer Science, Aberystwyth University, UK*

Abstract

We describe the first unambiguous evidence of enhanced Sodium on the lunar surface revealed by the Chandrayaan-1 X-ray Spectrometer (C1XS). The C1XS onboard the Chandrayaan-1 spacecraft was designed to map the surface elemental chemistry of the Moon using the X-ray fluorescence (XRF) technique. During the nine months of remote sensing observations (Nov'2008 - Aug'2009), C1XS measured XRF emission from the Moon under several solar flare conditions. A summary of entire C1XS observations and data selection methods are presented. Surface elemental abundances of major rock-forming elements viz., Mg, Al, Si and Ca as well as Na derived from C1XS data corresponding to certain nearside regions of the Moon are reported here. We also present a detailed description of the analysis techniques including derivation of XRF line fluxes and conversion to elemental abundances. The derived abundances of Na (2-3 wt%) are significantly higher than what has been known from earlier studies. We compare the surface chemistry of C1XS observed regions with the highly silicic compositions (intermediate plagioclase) measured by the Diviner Radiometer instrument onboard Lunar Reconnaissance Orbiter(LRO) in those regions.

Keywords: X-ray Fluorescence(XRF), Chandrayaan-1, C1XS, lunar surface chemistry

1 **1. Introduction**

2 Study of lunar surface chemistry is essential in understanding the forma-
3 tion and evolution of lunar crust and interior under different geochemical
4 processes on the Moon. The lunar surface has been explored extensively
5 through returned samples from the Apollo and Luna missions and through
6 orbital remote sensing measurements in multi-wavelengths. Since different
7 elements undergo different geochemical processes, the lunar surface chem-
8 istry is generally studied from the observation of major types of minerals on
9 the Moon. Surface mineralogy is inferred through visible and near-Infrared
10 (IR) spectroscopy. High resolution global lunar mineral maps are available
11 from various instruments such as the Ultraviolet-Visible (UV/VIS) multi-
12 spectral camera and Near IR camera on Clementine (Nozette et al., 1994;
13 McEwen & Robinson, 1997), the Spectral Profiler (SP) and Multiband Im-
14 ager (MI) on Kaguya (Manabu Kato et al., 2010; Ohtake et al., 2008) and
15 the HyperSpectral Imager (HySI) and Moon Mineralogical Mapper (M³) on
16 Chandrayaan-1 (Bhandari, 2005). Elemental abundances can be inferred
17 indirectly from Near IR spectroscopy which is primarily sensitive only to
18 Fe-bearing minerals. Diversity in the chemical composition of the Moon
19 is mostly addressed using these proxy lunar mineral maps. Recently, the
20 Diviner Lunar Radiometer experiment onboard the Lunar Reconnaissance

*Corresponding author at:

**Currently at Indian Institute of Astrophysics, Koramangala, Bangalore, India

Email address: athray@gmail.com (P.S. Athiray)

Preprint submitted to Planetary and Space Science

October 25, 2014

21 Orbiter (LRO) provided new insights to the iron-poor mineralogy of the
22 Moon using thermal IR spectroscopy (0.3 to 400 μm) (Paige et al., 2010).
23 Gamma-ray spectroscopy is also used to record gamma-ray spectra from
24 rock-forming and radio-active elements (Lawrence et al., 1998).
25 X-ray fluorescence (XRF) spectroscopy through remote sensing has a long
26 history in studying the chemical composition of atmosphere-free solar sys-
27 tem bodies (*for example, Apollo 15 (1971), Apollo 16 (1972) (Adler & Gerard,*
28 *1972; Adler et al., 1973a,b), Smart-1 (2003) (Grande et al., 2003), Kaguya*
29 *(2007) (Okada et al., 2008), Change-1 (2007) (Huixian et al., 2005) and*
30 *Chandrayaan-1 (2008) (Grande et al., 2009) for the Moon, Near Earth As-*
31 *teroid Rendezvous (NEAR) (1996) for the asteroid Eros (Trombka, 2000;*
32 *Nittler et al., 2001), HAYABUSA (2003) for the asteroid 25143 Itokawa*
33 *(Okada et al., 2006)). Solar X-rays excite surface elements of these bodies*
34 *to yield characteristic emission lines. X-ray remote sensing provides an un-*
35 *ambiguous and unique identification of elements. The upper-most layer of*
36 *the Moon (few 100 μm thick) is covered with lunar regolith - fine pulverized*
37 *grains of bedrock due to meteoritic bombardment. Interaction of soft X-rays*
38 *(1 - 10 keV) incident on the surface are limited to the top few microns on the*
39 *lunar surface (e.g., 2 microns for Na) in contrast to depths of centimeters to*
40 *tens of centimeters for gamma-rays. Thus X-ray remote sensing provides a*
41 *clean, direct and independent measure of elemental abundances which can*
42 *be compared with abundances derived from other spectral techniques. We*
43 *present new results from the most comprehensive analysis of data from the*
44 *Chandrayaan-1 X-ray Spectrometer (C1XS) experiment during many weak*
45 *solar flares.*

46 **2. Status of lunar surface chemical mapping**

47 The majority of our current knowledge on the chemical makeup of the
48 Moon is obtained from geochemical studies of returned lunar samples, aug-
49 mented by analyses of lunar meteorite samples collected from different
50 places on the earth. Adding to this are the direct remote sensing measure-
51 ments from different missions. Remote sensing in X-rays/or gamma-rays
52 provides the capability for direct chemical mapping of the Moon, but is
53 limited by the quantity and quality of the data. Since the Apollo era, sev-
54 eral lunar missions carried X-ray and gamma-ray experiments to map the
55 elemental abundances. However, a unified cross calibrated map does not
56 yet exist.

57 *2.1. Gamma ray mapping*

58 Characteristic gamma-rays are produced when high energy cosmic rays
59 interact with the nuclei of rock-forming elements. Abundances of light ma-
60 jor elements viz., Ca, Si, Al, Mg, O are derived indirectly due to strong
61 dependency on neutron production as well as changes in the lunar sub-
62 surface neutron flux (Yamashita et al., 2008). Furthermore, gamma-ray
63 data exhibit a complex and highly uncertain background arising from var-
64 ious sources (Zhang et al., 2012). Global maps of various rock-forming
65 and radio-active elements are available from the Gamma Ray Spectrometer
66 (GRS) onboard Lunar Prospector (LP) (Lawrence et al., 1998). Recently,
67 the global distribution of Ca abundance on the Moon has been obtained
68 from the GRS data from Kaguya (Yamashita et al., 2012). However, the
69 accuracy of abundances from GRS data is limited since the blending of the
70 lines and the mix of physical processes make the analysis uncertain.

71 2.2. X-ray mapping

72 The surface chemistry of the Moon can be studied from the character-
73 istic X-ray line intensities of different elements, emitted under solar X-ray
74 bombardment. Simultaneous measure of the incident solar X-ray spectrum
75 is essential for deriving elemental abundances. Major dependencies such as
76 matrix effects, geometry and elastic scattering of solar X-rays also have
77 to be considered for precise elemental analysis. Other factors affecting
78 the line intensity such as sample inhomogeneity and particle size distri-
79 bution are difficult to characterize. XRF experiments in Apollo 15 and
80 16 (Adler & Gerard, 1972; Adler et al., 1973a,b) covered only 10% (Clark,
81 1979) of the area on the equatorial region on the nearside of the Moon
82 and estimated relative abundances with respect to Si. Other X-ray exper-
83 iments such as D-CIXS (Grande et al., 2003) onboard SMART-1 and XRS
84 onboard Kaguya (Okada et al., 2008, 2009) suffered from severe radiation
85 damage which restricted its ability to yield meaningful quantitative anal-
86 ysis. Hence there are no measures of absolute elemental abundances from
87 any earlier X-ray experiments.

88 C1XS reached and observed the Moon flawlessly without losing much
89 of its high spectral capability. Due to overall low solar activity in this
90 period, it could not produce global elemental maps of the Moon during its
91 short mission life of ≈ 9 months. Nevertheless, simultaneous observation
92 of multiple elements were seen during a few relatively weak flares. Most
93 interestingly, C1XS measured the direct detection of sodium from the lunar
94 surface.

95 3. C1XS observations

96 3.1. Overview of C1XS

97 C1XS (Howe et al., 2009; Grande et al., 2009), onboard Chandrayaan-
98 1, was designed to map the abundances of major rock-forming elements
99 on the lunar surface using the XRF technique. The extended solar mini-
100 mum that prevailed during the Chandrayaan-1 mission time-frame (Nov'08
101 - Aug'09), left C1XS with only a handful of solar flares (a few C, B and A
102 class flares) during which quantitative analysis could be carried out. C1XS
103 used an array of 24 Swept Charge Devices (SCDs) (Lowe et al., 2001), with
104 each of area 1 cm², to record the X-ray emission with energies of 0.8 to
105 10 keV. Spatial resolution for a single spectral observation varies from <50
106 km to >1000 km depending on spacecraft altitude and integration time.
107 Simultaneous observation of solar X-rays, in the energy range of 1.8 to 20
108 keV, impinging on the Moon, was obtained from the Si-PIN based X-ray
109 Solar Monitor (XSM) (Alha et al., 2009) also onboard Chandrayaan-1. A
110 detailed description of C1XS instrument, its observations, steps involved
111 in data reduction and spectral extraction are given in Narendranath et al.
112 (2011)(here onwards Paper-I).

113 3.2. Data selection

114 The light curve of the C1XS experiment for the entire mission is shown
115 in Fig. 1. The plot shows integrated C1XS counts in the energy range 1
116 keV - 10 keV (red color points in Fig. 1) plotted along with GOES solar
117 soft X-ray flux in the energy range 1.55 keV - 12.4 keV (blue color lines in
118 Fig. 1). It is clearly seen that the solar X-ray activity was very minimal
119 during the entire duration and was relatively active in X-rays only in the

120 month of July 2009, in contrast to other times. After careful examination
121 of all data, we adopted the following criteria in choosing good data from
122 C1XS observations:

123 **C1.** Identification of useful observations corresponding to solar flares

124 **C2.** Selection of good observation intervals where the observed data are not
125 contaminated by any sudden increase in the flux of charged particles

126 Many flare observations were filtered out due to contamination from charged
127 particles. Also flares below B3 (dashed lines in Fig. 1) are not considered
128 for analysis as lines corresponding to Ca, Ti and Fe are absent, resulting
129 in large errors in the derived abundance values. Analysis and results of the
130 biggest flare seen by C1XS (a C3 flare), which occurred on the 5th July 2009
131 are published in Paper I. Results from flare observations during the early
132 phase of the mission (12th December 2008 and 10th January 2009) are given
133 by (Weider et al., 2012). Here we discuss results from flare observations
134 made on the 4th, 6th and 8th July 2009 (\leq C1 class flares), as shown in
135 the inset of Fig. 1b, which satisfied the aforesaid criteria. Footprints of
136 these observations covered a large area on the nearside of the Moon (Fig.
137 2). The majority of these observations span over lunar southern latitudes
138 which include the relatively young impact crater Tycho and its rays. A
139 summary of good observation intervals chosen for analysis along with the
140 class of flares observed and their respective locations on the Moon are given
141 in Table 1

Table 1: Selected good observation intervals of C1XS data

Date/Time (UTC)	Class of solar flare	Description of observed region
4 th Jul'09 01:18:00-01:21:59	≈B3.5	• Nearside highland region - covered some portions of Tycho rays
6 th Jul'09 17:04:29-17:19:44	≈C1.1	• Nearside highland region - covered the crater Tycho and majority of its rays
8 th Jul'09 05:27:31-05:30:20	≈B4.2	• Nearside mixed region - from crater Capuanus to crater Campanus.

142 4. C1XS data analysis

143 C1XS observations can be broadly grouped into three types viz., back-
 144 ground observations, ie., when X-ray & particle events are not observed,
 145 flare observations and observations during high fluxes of charged particles.
 146 Light curves depicting these types of observations are shown in Fig. 3.
 147 Spectral analysis of weak flare observations is severely constrained by low
 148 signals, requiring that data from multiple ground pixels be summed. This
 149 leads to coarser spatial mapping. Following are the major steps involved in
 150 spectral analysis:

- 151 1. Build background spectrum appropriate for the observation
- 152 2. Derive scattered spectrum of solar flare, reflected off the lunar surface
- 153 3. Derive X-ray line fluxes corresponding to different elements through
 154 spectral analysis
- 155 4. Convert line fluxes to elemental abundances using specially developed
 156 inversion algorithms

157 *4.1. Background estimates*

158 Background emission in X-rays arises from various sources (Hall et al.,
 159 2008). Apart from cosmic X-rays, interaction of high energy charged parti-
 160 cles in lunar orbit with the instrument leads to production of X-rays which
 161 also contributes to the overall observed continuum background. The Moon
 162 encounters two major particle environments in a synodic month (29.6 days):

163 **(a) Solar wind & high energy cosmic ray particles (≈ 24 days):**

164 Continuous flux of protons and electrons with energies ranging from
 165 eV to GeV around the Moon contribute mainly to the observed steady
 166 X-ray background in C1XS.

167 **(b) Charged particles in the Earth's geotail (≈ 6 days):** The geotail

168 extends up to several hundreds of Earth radii and it primarily com-
 169 posed of energetic electrons with an average energy of 1 keV (increas-
 170 ing to several keV occasionally; (Prakash, 1975)). Sporadic release
 171 of accelerated charged particles during solar eruptive events can alter
 172 the background spectrum significantly. The accelerated charged par-
 173 ticles travel with different speeds and reach the Earth and the Moon
 174 at different times. Spectral contamination due to bursts of charged
 175 particles is clearly identified by enhanced counts observed in the C1XS
 176 light curve (refer Fig. 3c).

177 The Moon was coincidentally inside the geotail when flares occurred
 178 during the 1st week of July 2009. Data over a complete orbit, without
 179 particle contamination and with solar activity less than A class flare level
 180 (ie., $< 1 \times 10^{-8}$ W/m²) alone are considered for background estimation.

181 Some of the observations made on the 6th and 8th July 2009 satisfied this
182 condition and the time-averaged background X-ray spectrum used for our
183 current analysis is shown in Fig. 4. For comparison, spectral hardening due
184 to a sudden burst of charged particles inside the geo-tail is also shown in
185 Fig. 4.

186 *4.2. Scattering of solar X-rays*

187 Background subtracted C1XS spectra contain XRF lines along with elas-
188 tically scattered solar X-rays. In order to model the scattering component,
189 the incident solar spectra for the observed C1XS timings are obtained from
190 XSM data which was constantly observing the Sun. XSM spectral anal-
191 ysis is performed using the solar soft package (SSW) (Freeland & Handy,
192 1998) which uses solar models based on the CHIANTI5.2 (Dere et al., 1997;
193 Landi et al., 2006) atomic database and the best fit solar parameters (ie.,
194 temperature, emission measure and coronal abundances) are obtained. The
195 best spectral fit to one of the observed XSM spectra for a C1 class flare is
196 shown in Fig. 5 with its spectral components. Using the best fit solar model
197 we calculated the scattered solar component following the same approach
198 given in Paper I (sec. 6).

199 *4.3. XRF analysis*

200 Detailed spectral analyses are carried out using the X-ray spectral anal-
201 ysis package (XSPEC) (Arnaud, 1996), where the XRF lines are modeled
202 as Gaussian functions along with an estimated spectrum of scattered solar
203 emission corresponding to a location/time interval (included as table model

204 ¹). It was noticed that the presence of a 0.4 μm thick Al filter in front
 205 of the detector could possibly contaminate and yield excess counts at 1.5
 206 keV. Using C1XS ground calibration data (Narendranath et al., 2010), we
 207 applied a correction factor (≈ 0.15) to the detection efficiency at 1.5 keV
 208 and derived the XRF line flux of the elements. One of the best-fit C1XS
 209 spectra is shown in Fig. 7, with XRF lines indicated. Due to the relative
 210 weakness of the incident solar flares, XRF signatures of Ti & Fe are not
 211 visible in most of the observations.

212 Apart from lines of major rock-forming elements, C1XS has clearly ob-
 213 served the XRF signature of Na at ≈ 1.04 keV in many spectra. Earlier
 214 C1XS reports by (Narendranath et al., 2011) and (Weider et al., 2012) also
 215 discussed the detection of Na from the Moon. The former proposed the possi-
 216 bility of high Na content on the lunar surface, while the latter suggested
 217 that it could originate from the scattering of incident solar spectrum. XRF
 218 line fluxes of the elements, including Na (wherever observed), determined
 219 for different flare observations are compiled in Table 2.

220

221 4.4. Deriving elemental abundances

222 We developed an XRF inversion code *x2abundance* to convert the ob-
 223 served X-ray line flux to absolute elemental abundances, where a new ap-
 224 proach is adopted using Fundamental Parameter (FP) (Criss & Birks, 1968;
 225 Rousseau & Boivin, 1998) method. A detailed description of the algo-
 226 rithm of *x2abundance* along with assumptions and limitations are given

¹Table Model - A model in XSPEC can also be defined as a two column table (energy versus photon intensity at some specified binning) as opposed to an analytical form. The final model spectrum is calculated by interpolation across the bins.

227 by (Athiray et al., 2013a). The algorithm was validated rigorously using
228 laboratory-based XRF experiments on metal alloys and lunar analogous
229 rocks (Athiray et al., 2013b). Dependencies which affect XRF intensities
230 such as the incident spectrum (I_o), matrix effects and geometry effects are
231 all incorporated. However, the code assumes a flat, homogeneous surface
232 which is not the case in reality. Remote sensing XRF experiments mainly
233 sense the lunar regolith which comprises distribution of particle sizes rang-
234 ing from sub-micron-sized particles to cm-sized rocks (McKay et al., 1991).
235 The observed XRF intensity get affected by the distribution of particle
236 size, as the mean free path of soft X-rays is smaller than the mean particle
237 size of lunar regolith. Laboratory experiments by (Maruyama et al., 2008;
238 Näränen et al., 2008) shows that XRF intensity decreases with increasing
239 phase angles (angle between source-surface-detector) and increases with de-
240 creasing size of particles. However, this effect is expected to be small on
241 C1XS results where the ground pixel dimensions are large (hundreds of km)
242 and considers a large distribution of particle sizes (Weider et al., 2012). The
243 effect is further minimized with the use of flux fractions (line flux/sum of
244 the flux in all lines).

245 Elemental abundances along with uncertainties are determined using $x2abundance$,
246 where the uncertainties in line flux measurements are transformed to uncer-
247 tainties in abundance values following statistical methods. The abundances
248 of Ti & Fe are kept frozen to the weighted average values derived from the
249 C1XS C3 flare observation (5.0 wt% & 0.13 wt%) (Paper I), since they are
250 not seen in the present spectra due to weak flare excitation. The derived
251 elemental abundances along with 1σ uncertainties are given in Table 3.

252 5. Results & Discussion

253 With good spectral resolution, C1XS observed XRF lines of the major
254 rock-forming elements Mg, Al, Si and Ca from the Moon simultaneously,
255 as well as sodium for the first time. Due to inadequate solar activity and
256 reduced mission life C1XS could not achieve its objective of global lunar
257 elemental mapping. However, with the best available data, we have de-
258 termined the elemental abundances for the C1XS-sampled locations on the
259 lunar surface. Through rigorous spectral analysis, we have confirmed the
260 unambiguous detection of XRF emission of Na from the Moon. Abundances
261 derived for the 4th and 6th July observations clearly exhibit lunar highland
262 features with high Al and Ca abundances and low Mg abundances. Abun-
263 dances derived for the 8th July observation show high Al & Mg abundances
264 which confirms a mixed terrain of highlands and mare.

265 Elemental abundances derived from the LP GRS, for a large area encom-
266 passing the C1XS-observed regions (see dashed box in Fig. 2), are compared
267 with C1XS abundances for the same regions in Fig. 7(a). We have applied
268 the correction factor for the Al filter to our earlier published C3 flare data
269 and re-derived the elemental abundances, which are also included in the
270 plot. Fig. 7(a) shows that C1XS compositions along with 1σ uncertainties
271 match well with the distribution of abundances derived from remote sensing
272 gamma-ray observations. For comparison, Table 3 also includes the aver-
273 age composition of lunar soils from Apollo 16 mission (Haskin & Warren,
274 1991) and the average feldspathic highland terrane composition from lunar
275 meteorites (Korotev, 2003). It is clear that the derived abundances of Na
276 ($> 1 \text{ wt}\%$) are larger than what has been known so far ($< 1 \text{ wt}\%$). Also, our
277 results seem to suggest an inverse relation between Ca and Na abundances

278 Fig. 8. According to our present understanding of highland regions from
 279 the returned lunar samples and meteorite collections, there exists a strong
 280 positive correlation between Al and Ca abundances, as shown in Fig. 7(b)i
 281 (Demidova et al., 2007). The results from C1XS show a lower Ca abun-
 282 dance for the intervals where Na is observed and the correlation improves
 283 when Ca and Na abundances are added and compared against Al Fig. 7(b)ii.

284

285 **Lunar observations & Magma Ocean Theory** : Our current un-
 286 derstanding of lunar evolution is based on the Lunar Magma Ocean (LMO)
 287 theory (Taylor, 1982; Warren, 1985, 1990) which states that the Moon was
 288 mostly/partially molten in its past. Subsequently, elemental fractionation
 289 occurred during the cooling phase of the magma. The LMO theory ad-
 290 vocates the assumption of a global distribution of ferroan anorthosites.
 291 Ferroan anorthosites mostly consist of anorthosite rocks which are char-
 292 acterized by plagioclase feldspar minerals with high calcium content. It is
 293 thus assumed, that the lunar highland crust was formed from plagioclase
 294 feldspar, floating on a global magma ocean. This theory is completely based
 295 on the analysis of samples of ferroan anorthosites collected from a small area
 296 on the nearside highland region of the Moon. However, solid solutions of
 297 the plagioclase feldspar mineral group include calcic and sodic end members
 298 called anorthite ($\text{CaAl}_2\text{Si}_2\text{O}_8$) and albite ($\text{NaAlSi}_3\text{O}_8$) (Perkins, 2006). Also,
 299 different plagioclase minerals can be formed by varying the sodium/calcium
 300 content. Such minerals are considered to have intermediate plagioclase com-
 301 positions. Diversity in plagioclase composition is studied by a factor called
 302 Anorthite number (An#) which is defined as $\frac{Ca}{Ca+Na+K}$ in moles. Fig. 9
 303 shows different intermediate plagioclase minerals starting from high calcic

304 end member to high sodic end member. Studying the diversity of pla-
305 gioclase compositions in the lunar highlands is an outstanding question in
306 lunar science eg. (Donaldson Hanna et al., 2012a). This can be addressed
307 by mapping the distribution of anorthite content (An#) on the lunar high-
308 lands.

309

310 Global distribution of pure ferroan anorthosite (PAN) obtained from the
311 MI and SP instruments onboard SELENE, indicated high calcic plagioclase
312 feldspar ($>An_{95}$) (Ohtake et al., 2009) in the highland crust, in clear sup-
313 port of the LMO theory. It should be noted that both instruments were
314 operated in the NIR region where plagioclase with minor amounts of iron,
315 exhibits a broad absorption band centered around $1.25 \mu m$ owing to the
316 electronic transitions of Fe^{2+} . But NIR spectroscopy is less sensitive to
317 An# and hence cannot address the presence of calcic and sodic content in
318 plagioclase feldspar.

319

320 Thermal Infrared (TIR) spectroscopy has been extensively used in the
321 laboratory to study the variations in plagioclase minerals (Donaldson Hanna et al.,
322 2012b) using the position of Christiansen Frequency (CF), an emissivity
323 maximum that indicates the composition related to (An#). In silicate min-
324 erals, the emissivity maximum occurs around $8 \mu m$ when the real part of
325 refractive index approaches unity (Pieters, 1999). Ca-rich feldspathic anor-
326 thite exhibit CF positions around $7.84 \mu m$ whereas plagioclase with Na com-
327 ponent shift towards lower CF values $\leq 7.8 \mu m$ (Donaldson Hanna et al.,
328 2014). Ultramafic minerals exhibit intermediate and long CF values which
329 are indicated in the CF value map shown in Fig. 10. Using this diagnos-

330 tic feature, the Diviner instrument onboard the LRO identified intermedi-
331 ate plagioclase compositions (Greenhagen et al., 2010; Kusuma et al., 2012)
332 over numerous areas on the Moon which were shown to be pure plagioclase
333 feldspar using the NIR measurements of the MI and SP instruments. Fig. 10
334 shows the overplot of C1XS observed regions on the LRO diviner CF value
335 map. Some of the C1XS observed regions are likely to be dominated by the
336 impact ejecta and disturbed regolith due to the young impact crater Tycho.
337 It is clear that some of the regions observed by C1XS show unusual mineral
338 compositions. The An# values derived from C1XS abundances correspond
339 to intermediate plagioclase compositions such as labradorite and bytownite.
340 However the LMO theory predicts alkali depletion over the whole Moon as a
341 consequence of the moon-forming giant impact. The C1XS results indicat-
342 ing high Na content contradict the extreme loss of volatiles by vaporization.
343 There exist physical processes which do not require alkali depletion of the
344 bulk Moon (Nekvasil et al., 2013). These authors have also shown that the
345 bulk Moon could still retain alkali-rich contents under different tempera-
346 ture and pressure conditions. From our observations over the impact crater
347 Tycho and its rays, we suggest that the ejecta has excavated alkali-rich
348 material from deep layers of the bulk Moon. Suggestive evidences are also
349 seen in Diviner images showing unusual compositions over relatively young
350 impact craters. The first results from the Ultraviolet-Visible Spectrometer
351 (UVS) onboard LADEE (The Lunar Atmosphere and Dust Environment
352 Explorer) measured spatial and temporal variations of Na flux in the ex-
353 osphere (Colaprete et al., 2014). Associations with surface compositions,
354 meteorites etc., are being examined and could pave the way for further
355 confirmation.

356 6. Conclusion

357 To summarize, the C1XS experiment performed extremely well and
358 proved its capability by distinctly observing XRF lines of rock-forming ele-
359 ments from the Moon. In this paper, we have presented a detailed descrip-
360 tion of the entire C1XS observation data. Due to lack of confidence, earlier
361 quantitative elemental estimates for certain selected flare observations (5th
362 Jul'09, 12th Dec'08 & 10th Jan'09) made by (Narendranath et al., 2011;
363 Weider et al., 2012) did not include Na. Based on the selection criteria and
364 spectral analysis steps described here, we clearly showed the unambiguous
365 direct detection of Na from the Moon. Further, we also determined the
366 elemental abundances, including Na for the first time, for additional flare
367 observations on the 4th, 6th & 8th Jul'09. The derived abundances of sodium
368 are significantly larger than what has been known from earlier studies of
369 lunar materials. The compositions determined from C1XS tend to support
370 recent theories and findings of intermediate plagioclase on the Moon. How-
371 ever, precise Ca and Na abundance measurements are required on a global
372 scale to address the evolution of the lunar surface. In this regard, the qual-
373 itative and quantitative study of Na abundance by X-rays will be one of
374 the prime science objectives of the CLASS instrument on India's upcoming
375 second mission to the Moon, Chandrayaan-2.

376

377 7. Acknowledgments

378 We thank the anonymous referee whose edits and suggestions greatly
379 improved the paper.

- 380 Adler, I. et al., 1973. Results of the Apollo 15 and 16 X-ray experiment. *Geochim.*
381 *Cosmochim. Acta*, 3, 2783-2801.
- 382 Adler, I. et al., 1973. Apollo 15 and 16 results of the integrated geochemical experiment.
383 *The Moon*, 7, 487-504
- 384 Adler, I., Gerard, J., 1972. The Apollo 15 X-ray fluorescence experiment. *Geochim.*
385 *Cosmochim. Acta*, 3, 2157-2178
- 386 Alha, L. et al., 2009. Ground calibration of the Chandrayaan-1 X-ray Solar Monitor
387 (XSM). *Nucl. Instr. Meth. A*, 607, 544-553.
- 388 Arnaud, K.A., 1996. XSPEC: The first ten years. *ASP Conf. Ser.* 101, 170-20.
- 389 Athiray, P. S. et al., 2013a. Validation of methodology to derive elemental abundances
390 from X-ray observations on Chandrayaan-1, *Planet. Space Sci.*, 75, 188-194.
- 391 Athiray, P. S. et al., 2013b. Experimental validation of XRF inversion code for
392 Chandrayaan-1, *Planet. Space Sci.*, 89, 183-187.
- 393 Bhandari, N., 2005. Chandrayaan-1: Science goals, *J. Earth system Sci.*, 114, 701-709.
- 394 Pieters, 1999. Lunar materials from the visible to mid-infrared : The effects of space
395 weathering. *Planetary petrology and geochemistry*, 243 - 250.
- 396 Clark, P.E., 1979. Correction, Correlation and Theoretical Intensity Consideration of Lu-
397 nar X-ray Fluorescence Intensity Ratios. PhD thesis. University of Maryland, Mary-
398 land, USA
- 399 Colaprete, A. et al., 2014. Overview of the LADEE Ultraviolet-Visible Spectrometer:
400 Design, Operations and Initial results. 45th Conference on the Lunar and Planet. Sci.,
401 2566.
- 402 Criss, J.W., Birks, L.S., 1968. Calculation methods for fluorescent X-ray Spectrometry:
403 Empirical coefficients vs fundamental parameters. *Anal. Chem.*, 40, 1080-1088.
- 404 Demidova, S. I. et al., 2007. Chemical composition of lunar meteorites and the lunar
405 crust. *Petrology*, 15, 386-407.
- 406 Dere, K. P., et al., 1997. CHIANTI - An atomic database for emission lines. *Astron.*
407 *Astrophys.*, 129, 149-173.
- 408 Dexter Perkins, *Mineralogy*, Second Edition, Pearson Prentice Hall. (2006).
- 409 Donaldson Hanna, K.L. et al., 2014. Global assessment of pure crystalline plagioclase
410 across the Moon and implications for the evolution of the primary crust, *J. Geophys.*

- 411 Res. Planets, 119, 1516-1545.
- 412 Donaldson Hanna, K. L. et al., 2012a. Compositional diversity of crystalline plagioclase
413 in the lunar highlands. 2nd Conference on the Lunar Highlands Crust , 9024.
- 414 Donaldson Hanna, K.L. et al., 2012b. Laboratory emissivity measurements of the plagioclase
415 solid solution series under varying environmental conditions. J. Geophys. Res.
416 Planets, 117, E11004.
- 417 Freeland, S. L., and Handy, B. N., 1998. Data analysis with the solar soft system. Sol.
418 Phys., 182, 497-500
- 419 Grande, M., et al., 2009. The C1XS X-ray Spectrometer on Chandrayaan-1. Planet.
420 Space Sci., 57, 717-724.
- 421 Grande, M., et al., 2003. The D-CIXS X-ray mapping spectrometer on SMART-1. Planet.
422 Space Sci., 51, 427-433.
- 423 Greenhagen, B. T. et al., 2010. Global Silicate Mineralogy of the Moon from the Diviner
424 Lunar Radiometer. Science, 329, 1507-1509.
- 425 Hall, D. et al., 2008. Simulating and reproducing instrument background for X-ray CCD
426 spectrometers in space. Proc. SPIE, 7021, 58-69.
- 427 Howe, C. J., et al., 2009. Chandrayaan-1 X-ray Spectrometer (C1XS) instrument design
428 & technical details. Planet. Space Sci., 57, 735-743.
- 429 Korotev, L. R. et al., 2003. Feldspathic lunar meteorites and their implications for com-
430 positional remote sensing of the lunar surface and the composition of the lunar crust.
431 Geochim. Cosmochim. Acta, 667, 4895-4923.
- 432 Kusuma, K. N. et al., 2012. Geochemical and mineralogical analysis of Gruithuisen region
433 on Moon using M3 and DIVINER images., Planet. Sp. Sci., 67, 46-56.
- 434 Landi, E. et al., 2006. CHIANTI - An atomic database for emission lines VII: New data
435 for X-rays and other improvements. Astrophys. J., 162, 261-280.
- 436 Larry Haskin and Paul Warren, 1991. Lunar Chemistry, Lunar Source Book, p 357-474.
- 437 Huixian et al., 2005. Scientific objectives and payloads of Chang'E-1 lunar satellite. J.
438 Earth Sys. Sci. 114, 789.
- 439 Larry R. Nittler., et al., 2001. X-ray fluorescence measurements of the surface elemental
440 composition of asteroid 433 Eros. Met. Plan. Sci., 36, 1673-1695.
- 441 Lawrence, D.J. et al., 1998. Global elemental maps of the Moon: The Lunar Prospector

- 442 gamma-ray spectrometer. *Science*, 281, 1484-1489.
- 443 Lowe, B. G., et al., 2001. The swept charge device, a novel CCD-based EDX detector:
444 First results. *Nucl. Instr. Meth. A*, 458, 568-579.
- 445 Lucey, G. P., 1998. Model near-infrared optical constants of olivine and pyroxene as a
446 function of iron content. *J. Geophys. Res.* 103, 1703-1713.
- 447 Manabu Kato et al., 2010. The Kaguya Mission Overview. *Sp. Sci. Rev.* 154, 3-19.
- 448 Maruyama, Y., et al., 2008. Laboratory experiments of particle size effect in X-ray fluo-
449 rescence and implications to remote X-ray spectrometry of lunar regolith surface. *Ear.*
450 *Planets Space*, 60, 293-297.
- 451 McKay, D. S., et al., 1991. *Lunar Source Book: A Users Guide to the Moon*. Cambridge
452 Univ. Press, pp. 285-356.
- 453 McEwen, A.S. and Robinson. M, 1997. Mapping of the Moon by Clementine. *Adv. Sp.*
454 *Res.* 19, 1523-1533.
- 455 Näränen, J. et al., 2008. Laboratory studies into the effect of regolith on planetary X-ray
456 fluorescence spectroscopy. *Icarus*, 198, 408-419.
- 457 Narendranath, S. et al., 2010. Calibration of the C1XS Instrument on Chandrayaan-1.
458 *Nucl. Instr. Meth. A*, 621, 344-353.
- 459 Narendranath, S. et al., 2011. Lunar X-ray fluorescence observations by the Chandrayaan-
460 1 X-ray Spectrometer (C1XS): Results from the nearside southern highlands. *ICARUS*,
461 214, 53-66.
- 462 Nekvasil, H. et al., 2013. Alkali depletion of the bulk Moon, Is it required?. *Proc. Lunar*
463 *Planet. Sci. Conf.*, 44, 2830.
- 464 Nozette, S. et al., 1994. The Clementine Mission to the Moon - Scientific Overview.
465 *Science* 266, 1835-1839
- 466 Ohtake, M. et al., 2008. Performance and scientific objectives of the SELENE (KAGUYA)
467 Multiband Imager. *Earth Planets Space* 60, 257-264.
- 468 Ohtake, M. et al., 2009. The global distribution of pure anorthosite on the Moon. *Nature*,
469 461, 236-241.
- 470 Okada, T. et al., 2006. X-ray fluorescence spectrometry of Asteroid Itokawa by Hayabusa.
471 *Science* 312, 1338134 orbiter. *Earth Plan. Space*, 60, 277-281.
- 472 Okada, T. et al., 2008. Instrumentation and performance evaluation of the XRRS on

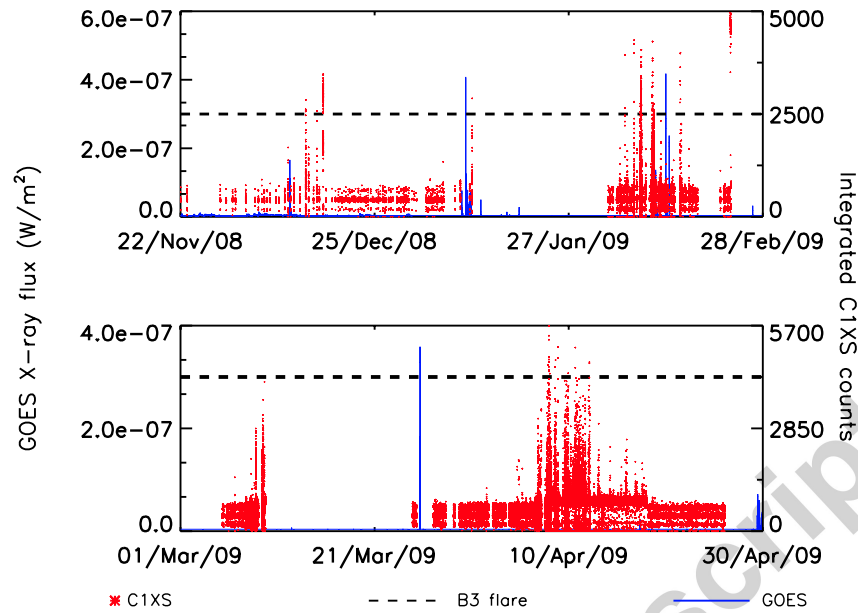
- 473 SELENE orbiter. *Earth Plan. Space*, 60, 277-281.
- 474 Okada, T. et al., 2009. X-ray fluorescence spectrometer (XRS) on kaguya: Current status
475 and results. *Proc. Lunar Planet. Sci. Conf.*, 40, 1897.
- 476 Paige, D. A. et al., 2010. The Lunar Reconnaissance Orbiter Diviner Lunar Radiometer
477 Experiment. *Space Sci. Rev.*, 150, 125-160.
- 478 Prakash, A. 1975, Magnetospheric protons and electrons encountered by the Moon in
479 the plasma sheet. *The Moon*, 14, 71-78.
- 480 Prettyman, T. H. et al., 2006. Elemental composition of the lunar surface: Analysis of
481 gamma ray spectroscopy data from Lunar Prospector, *J. Geophys. Res.* 111, 12007-
482 12048.
- 483 Rousseau, R., Boivin, J., 1998. The fundamental algorithm: A natural extension of
484 Sherman equation. *The Rigaku J.*, 15, 13-28.
- 485 Taylor, S. R., 1982. *Planetary Science: A Lunar Perspective* (Lunar and Planetary In-
486 stitute).
- 487 Trombka, J. I., 2000. The elemental composition of Asteroid 433 Eros: Results of the
488 NEAR-Shoemaker X-ray Spectrometer, *Sci.*, 289, 2101-2105.
- 489 Warren, P. H., 1985. The Magma Ocean Concept and Lunar Evolution. *Ann. Rev. Ear.*
490 *Pla. Sciences*, 13, 201-240.
- 491 Warren, P. H., 1990. Lunar anorthosites and the magma-ocean plagioclase-flotation hy-
492 potheses: importance of FeO enrichment in the parent magma. *Am. Mineral*, 75,
493 46-58.
- 494 Weider, S. Z., et al., 2012. The Chandrayaan-1 X-ray Spectrometer : First results. *Planet.*
495 *Space Sci.*, 60, 217-228.
- 496 Yamashita, N. et al., 2008. Complexities of gamma-ray line intensities from the lunar
497 surface. *Earth Planet Sp.*, 60, 313-319.
- 498 Yamashita, N. et al., 2012. The global distribution of calcium on the Moon : Implications
499 for high-Ca pyroxene in the eastern mare region. *Earth and Planet. Sci., Let.*, 353,
500 93-98.
- 501 Zhang Liyan, et al., 2012. Background deduction of the Chang'E-1 gamma-ray spectrom-
502 eter data. *Chinese J. Geochem.* 31, 234-241.

Table 2: X-ray line flux (photons/cm²/s) from C1XS spectral analysis with 1σ errors. Approximate central co-ordinates of each ground pixel are given in the first column

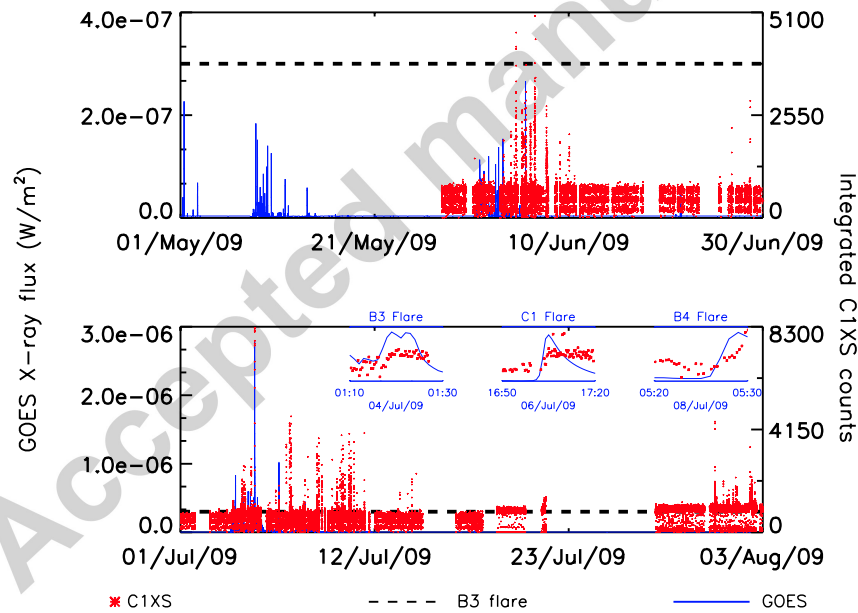
Lat , Lon	Date	Na K α	Mg K α	Al K α	Si K α	Ca K α
Time in UTC						
-45.2 , 25.0	04/07/09	-	0.54 \pm	1.03 \pm	0.83 \pm	0.08 \pm
	01:18:00 - 01:21:59	-	0.06	0.08	0.06	0.01
-30.2 , 25.0	04/07/09	0.72 \pm	0.83 \pm	1.59 \pm	1.06 \pm	0.06 \pm
	01:22:00 - 01:27:09	0.15	0.07	0.09	0.06	0.01
-63.2 , -10.5	06/07/09	-	0.92 \pm	1.54 \pm	0.94 \pm	0.18 \pm
	17:04:29 - 17:06:26	-	0.07	0.07	0.05	0.02
-53.2 , -10.5	06/07/09	0.56 \pm	1.26 \pm	2.10 \pm	1.46 \pm	0.12 \pm
	17:06:27 - 17:10:17	0.13	0.17	0.11	0.07	0.01
-43.0 , -10.5	06/07/09	0.73 \pm	1.30 \pm	2.08 \pm	1.31 \pm	0.04 \pm
	17:10:47 - 17:13:59	0.16	0.10	0.13	0.09	0.01
-30.7 , -10.3	06/07/09	-	0.88 \pm	1.40 \pm	1.08 \pm	0.02 \pm
	17:14:11 - 17:19:44	-	0.15	0.06	0.05	0.01
-30.0 , -28.7	08/07/09	0.45 \pm	0.73 \pm	0.92 \pm	0.42 \pm	0.03 \pm
	05:27:31 - 05:30:20	0.22	0.05	0.04	0.02	0.01

Table 3: Elemental abundances (wt%) from C1XS analysis with 1σ uncertainties

Lat , Lon	Na	Mg	Al	Si	Ca
-45.2 , 25.0	-	4^{+1}_{-1}	16^{+1}_{-1}	18^{+1}_{-1}	13^{+1}_{-1}
-30.2 , 25.0	3^{+1}_{-1}	4^{+1}_{-1}	17^{+1}_{-1}	17^{+1}_{-1}	10^{+1}_{-1}
-63.2 , -10.5	-	6^{+1}_{-1}	18^{+1}_{-1}	13^{+1}_{-1}	14^{+1}_{-1}
-53.2 , -10.5	2^{+1}_{-1}	6^{+1}_{-1}	17^{+1}_{-1}	16^{+1}_{-1}	10^{+1}_{-1}
-43.0 , -10.5	3^{+1}_{-1}	5^{+1}_{-1}	17^{+1}_{-1}	18^{+1}_{-1}	8^{+1}_{-1}
-30.7 , -10.3	-	4^{+2}_{-1}	16^{+2}_{-1}	23^{+3}_{-2}	8^{+2}_{-3}
-30.0 , -28.7	5^{+0}_{-1}	9^{+1}_{-2}	15^{+2}_{-2}	16^{+2}_{-1}	6^{+1}_{-1}
Average feldspathic meteorite compositions	0.26	3.26	14.92	20.89	11.65
AP16 (Soil & Regolith Breccia Average)	0.35	3.62	14.41	20.98	10.41
LP average (dashed box Fig. 2)	-	5.32	13.28	20.23	10.96



(a) Nov'2008 - Apr'2009



(b) May'2009 - Aug'2009

Figure 1: The entire mission light curve of C1XS experiment from 22nd Nov.2008 - 3rd Aug.2009. The solar soft X-ray flux from the GOES satellite indicates the X-ray activity of the Sun during the life time of the mission. Useful C1XS observations are during solar flares with intensity B3 ($3 \times 10^{-7} \text{ W/m}^2$) and above which is marked as dashed line. Red points indicate C1XS integrated counts with a time bin of 16s; Blue lines indicate solar X-ray flux with a time bin of 1min. Flare observations discussed in this paper are shown in the inset of Fig. 1b.

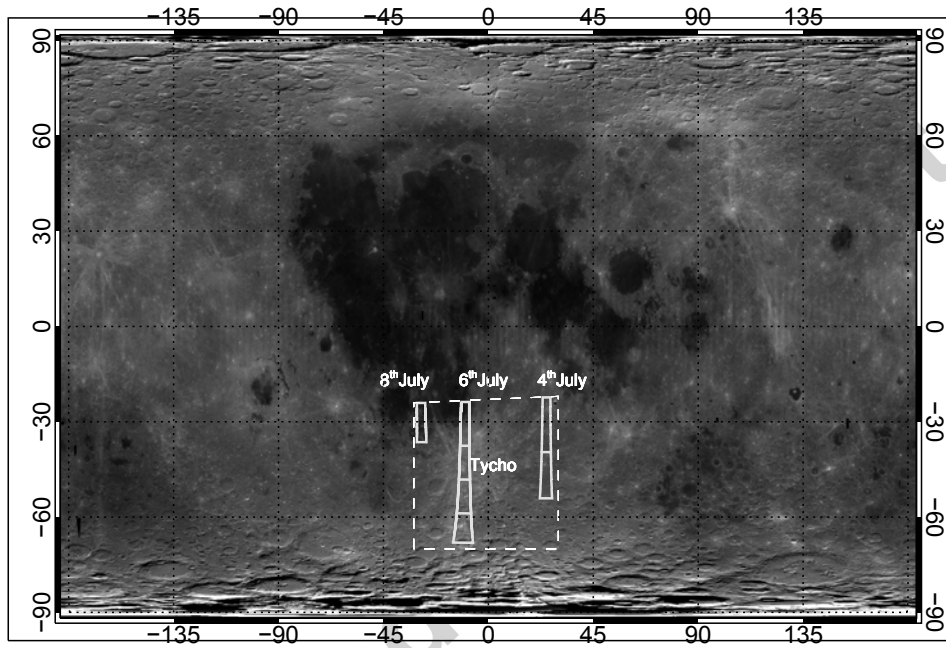


Figure 2: Ground-track of C1XS observations made on 4th, 6th and 8th July 2009 plotted over the Clementine lunar albedo map (750nm). Elemental abundances from the LP gamma-ray data used for comparison are taken from the region of interest shown as dashed line box which encompass C1XS observed locations

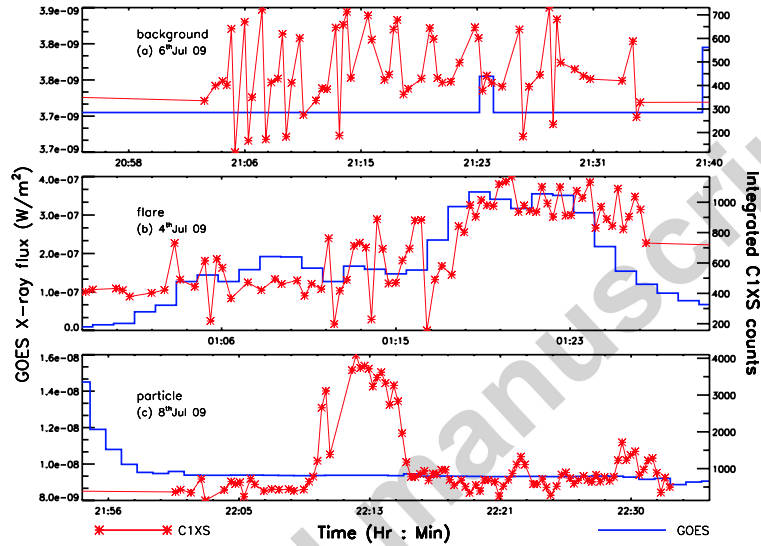


Figure 3: Light curves showing C1XS integrated counts (1 keV - 10 keV) (*Red line-points*) along with X-ray solar flux obtained from GOES (1.55 keV - 12.4 keV) (*blue lines*) (a) background observation - without solar flare and high particle flux (b) flare observation showing a rise in solar flux and C1XS counts (c) particle hit observation indicated by a sudden rise in the C1XS counts without any corresponding increase in the solar flux

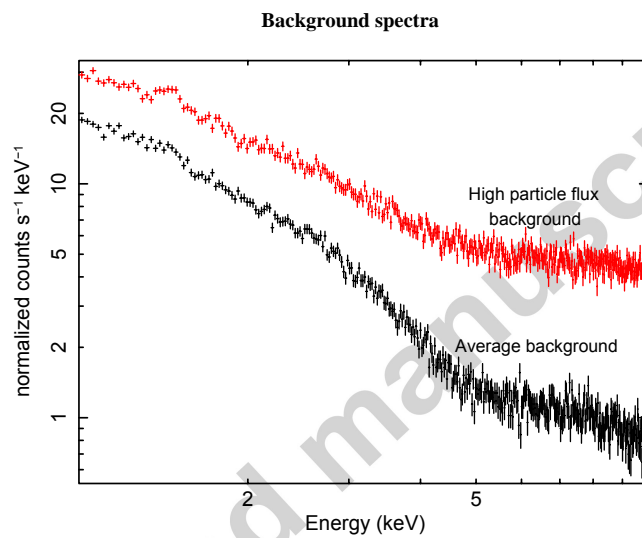


Figure 4: C1XS average background spectrum inside the geotail measured from multiple orbits during the month of July 2009 used for data analysis along with a spectrum corresponding to high particle flux (red color points).

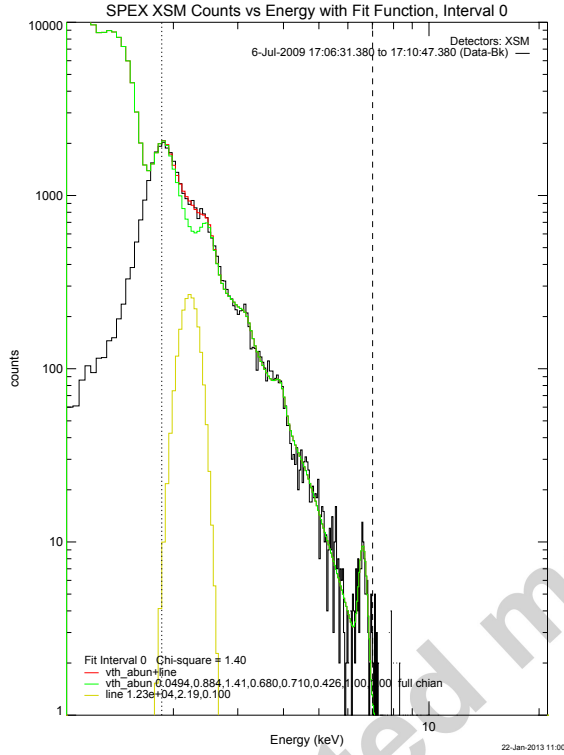


Figure 5: Best fit to one of the solar spectra observed by the XSM on 6th July 2009, using the CHIANTI database. The observed continuum spectrum along with the ionized solar coronal emission lines are well modeled using *vtherm_abund* in OSPEX (Object Spectral Executive - an interface tool for solar X-ray data analysis in SSW) (Green line). Further, a Gaussian component is fitted at ≈ 2.1 keV (Yellow line) for improved fit. Red line represents the combined spectral fit and data points are in Black.

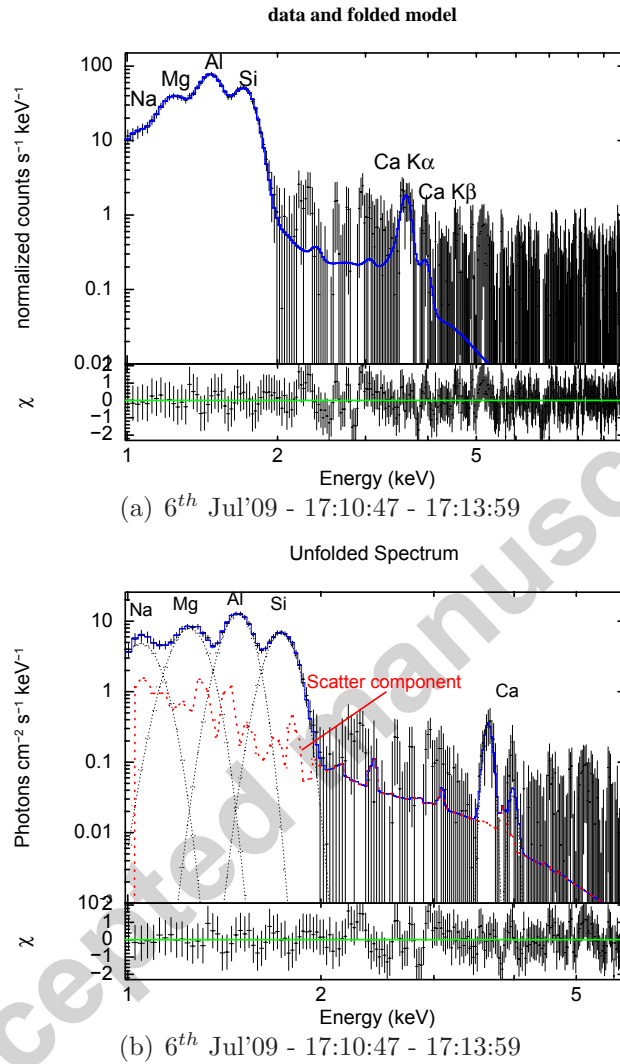
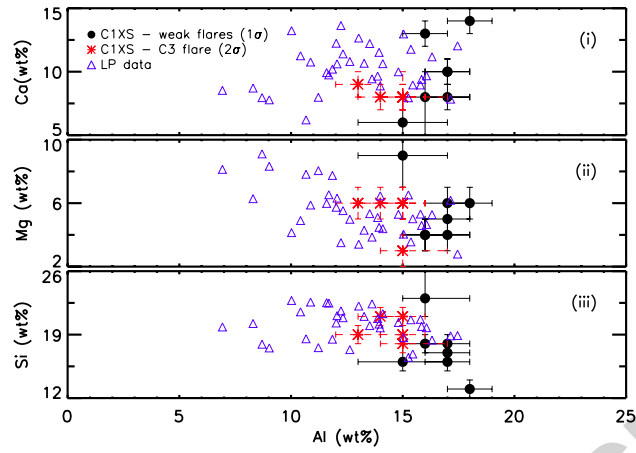
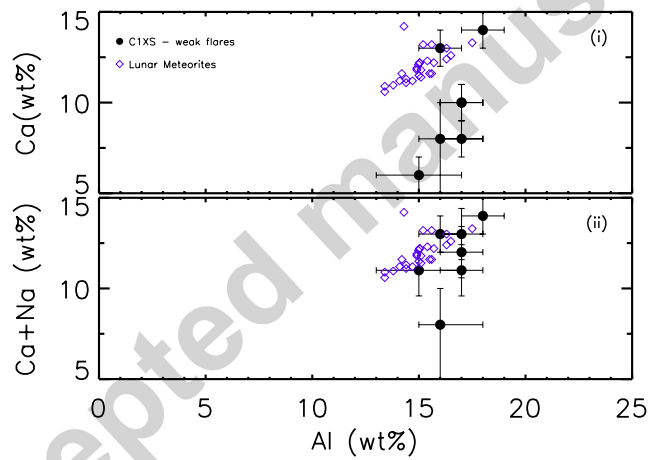


Figure 6: Best fit for the observed XRF spectrum for an interval during C1 class flare, with all components. Data points (black) are shown with error bars; XRF lines of major elements are marked. Residuals of fit (difference between model and data) in terms of 1σ error bar size are shown in the bottom panel of each figure. (a) Spectral fit convolved with detectors' response (b) Deconvolved photon spectrum corresponding to the best fit.



(a) C1XS abundances vs LP abundances



(b) C1XS abundances vs Lunar Meteorite abundances

Figure 7: Comparison of C1XS abundance with (a) GRS data from Lunar Prospector (Prettyman et al., 2006). (b) Lunar Meteorite compositions (Demidova et al., 2007). C1XS predict low Ca abundance in comparison to the correlation established between Al & Ca in lunar meteorite collections (i). Sum of Na & Ca abundances agree well with the correlation (ii).

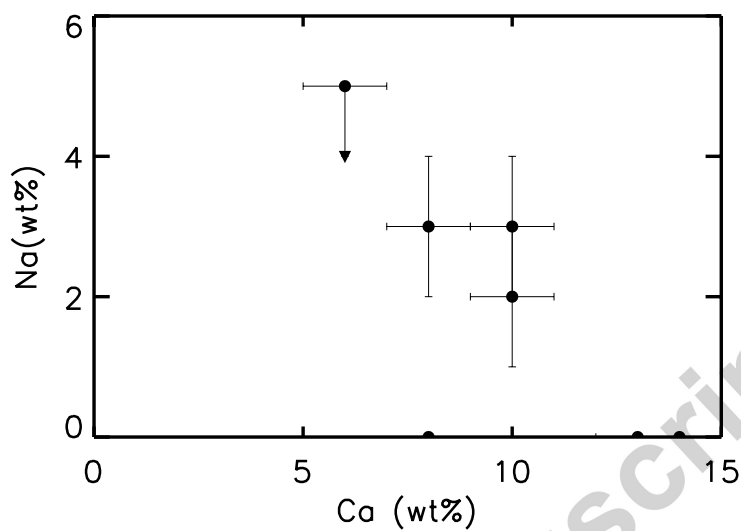


Figure 8: Relation between Ca and Na abundances from CIXS observations. The point with inverted arrow is the upper-limit of Na abundance for that observation

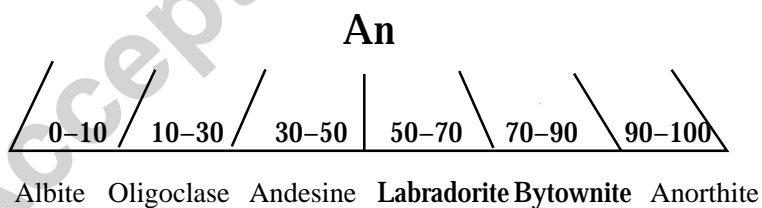


Figure 9: Plagioclase solutions from calcic end member to sodic end member which are called intermediate plagioclase minerals referred by An#.

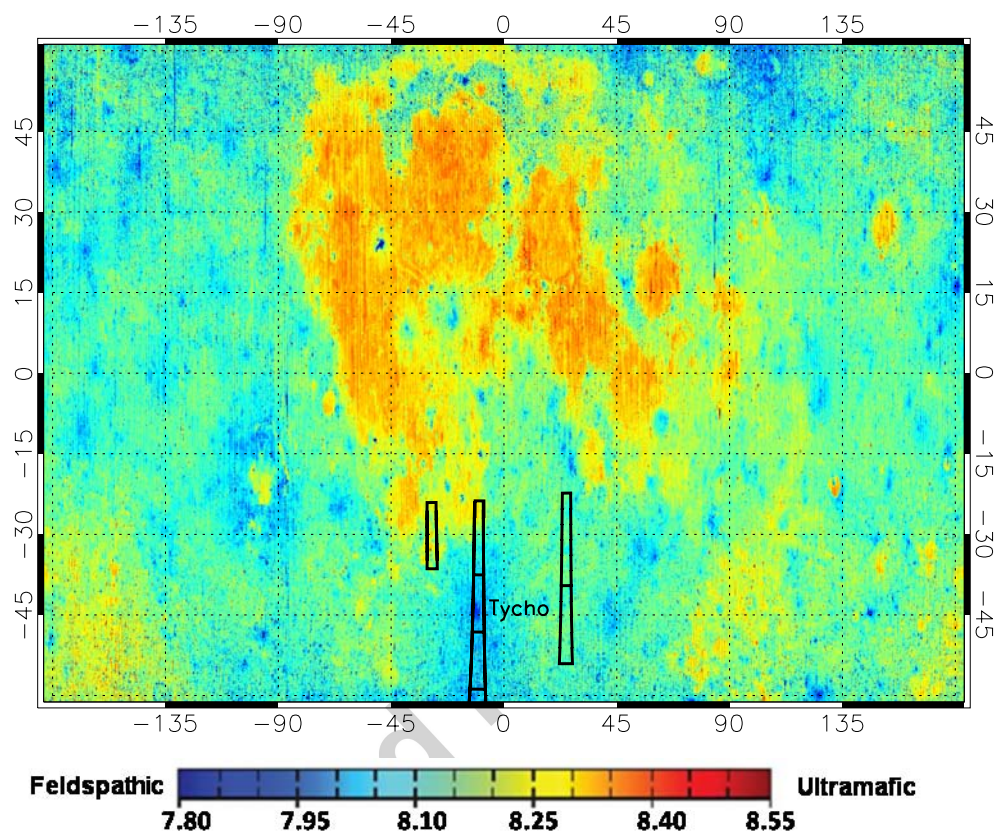


Figure 10: Track of C1XS observed region on the Moon - 4th, 6th and 8th July 2009 plotted over the LRO Diviner radiometer Christiansen Feature (CF) value map (in μm). Ca-rich plagioclase have CF positions around $7.84 \mu\text{m}$ whereas plagioclase with Na component shift towards low CF values ($\leq 7.8 \mu\text{m}$). Mafic minerals such as pyroxene, olivine show long CF values as indicated in the color map. Some of the saturate blue regions in the map with lower CF values represent unusual compositions (Greenhagen et al., 2010).